Anomalous dynamics of interstitial dopants in soft crystals

Justin Tauber[a,1], Ruben Higler[a,1], and Joris Sprakel[a,2]

[a]Physical Chemistry and Soft Matter, Wageningen University & Research, 6708 WE Wageningen, The Netherlands

Edited by Pablo G. Debenedetti, Princeton University, Princeton, NJ, and approved October 12, 2016 (received for review June 20, 2016)

The dynamics of interstitial dopants govern the properties of a wide variety of doped crystalline materials. To describe the hopping dynamics of such interstitial impurities, classical approaches often assume that dopant particles do not interact and travel through a static potential energy landscape. Here we show, using computer simulations, how these assumptions and the resulting predictions from classical Eyring-type theories break down in entropically stabilized body-centered cubic (BCC) crystals due to the thermal excitations of the crystalline matrix. Deviations are particularly severe close to melting where the lattice becomes weak and dopant dynamics exhibit strongly localized and heterogeneous dynamics. We attribute these anomalies to the failure of both assumptions underlying the classical description: (*i*) The instantaneous potential field experienced by dopants becomes largely disordered due to thermal fluctuations and (*ii*) elastic interactions cause strong dopant–dopant interactions even at low doping fractions. These results illustrate how describing nonclassical dopant dynamics requires taking the effective disordered potential energy landscape of strongly excited crystals and dopant–dopant interactions into account.

anomalous dynamics | doping | crystals

Doping pure crystalline solids with small amounts of interstitial impurities is a widely used method to enhance material properties such as heat and electric conductivity (1–4) or to tailor mechanical properties (5). Prototypical examples include the introduction of carbon atoms in iron crystals to make steel or the doping of plastic crystals with Li ions to create solid-state batteries (4). To ensure longevity of doped materials, it is essential that the spatial homogeneity and transport dynamics of the dopants within the crystal are well controlled and understood. Although theories and models are abundant (5–11), it remains unclear how large thermal excitations of the matrix lattice affect the dynamics of dopants. This becomes of particular interest during the processing of doped crystals, where they are heated close to or beyond their melting point. For example in body-centered cubic (BCC) iron doped with carbon, significant deviations from the exponential increase of diffusivity with temperature, expected from Arrhenius' law, are observed close to the melting temperature where lattice excitations are strong (12). Whereas doping is typically performed to tailor material properties at the macroscopic scale, these enhanced properties emerge from the dynamics and interactions between dopants at the scale of individual atoms (13). In classical theories for dopant dynamics, impurity particles are described as hopping through a potential energy landscape that is set by a perfect lattice symmetry, with transition rates governed by the energy barriers between adjacent interstitial sites and their occupancy (6, 7, 14). In reality, thermal fluctuations of atoms away from their equilibrium lattice positions will randomize the instantaneous potential energy landscape that the dopants experience; this action could lead to failure of classical approaches to capture the physics of impurity diffusion when lattice excitations become pronounced. This failure may be particularly severe for crystals of the BCC symmetry, such as the high-temperature lattice of sodium, lithium, and iron. In these high-temperature BCC phases, thermal fluctuations are large due to the relatively low coordination number; in fact, these fluctuations increase the entropy of the solid to such an extent that they are responsible for its thermodynamic stability (15). For impurity transport in structurally disordered colloidal glasses, it was recently shown that thermal fluctuations that create time variations in the potential energy landscape can have a strong effect on the dopant diffusivity (16, 17); yet these effects remain largely unexplored for very soft crystals that exhibit an on-average ordered lattice.

In this paper we study the dynamics of interstitial dopants in BCC crystals prepared from colloidal particles interacting by long-ranged electrostatic interactions. Using Brownian dynamics simulations we probe in detail how strong thermal fluctuations of the base crystal affect the spatial homogeneity of the dopants and their motion through the lattice. Dopants within a static base crystal obey quantitative predictions of classical transition-state theory; by contrast, the same impurities diffusing in a fluctuating crystal exhibit completely different behavior. We show how thermal excitation of the lattice causes clustering of the interstitials while simultaneously giving rise to strong disorder in the instantaneous potential energy landscape. This results in heterogeneous and anomalous dynamics of interstitials within an on-average perfect lattice. We support these observations with direct imaging experiments on a colloidal system, using confocal microscopy. These data illustrate how large thermal fluctuations can give rise to heterogeneous dynamics in ordered solids, which cannot be captured by classical hopping theories.

The classical approach to describe the diffusion of interstitial impurities through a crystalline matrix starts with the assumption that the dopants experience a static potential energy landscape

Significance

Doping crystalline solids with small impurity atoms is a common approach to tailor material properties, for example to increase mechanical toughness in making steel or to create solid-state batteries. The properties and longevity of doped materials depend sensitively on the spatial distribution and dynamics of the dopants within the lattice. In this paper we show how classical approaches to predict dopant dynamics fail in crystals approaching their melting point. Thermal excitation of the, on-average perfect, lattice breaks local inversion symmetry, causing an instantaneous disordered potential field. As a consequence, the dopants exhibit anomalous and heterogeneous dynamics within an ordered solid. This result sheds unique light on the complex behavior of doped materials that cannot be explained using classical lattice theories.

Author contributions: J.T., R.H., and J.S. designed research; J.T. and R.H. performed research; J.T. and R.H. analyzed data; and J.T., R.H., and J.S. wrote the paper.

The authors declare no conflict of interest.

This article is a PNAS Direct Submission.

Freely available online through the PNAS open access option.

[1]J.T. and R.H. contributed equally to this work.

[2]To whom correspondence should be addressed. Email: joris.sprakel@wur.nl.

This article contains supporting information online at www.pnas.org/lookup/suppl/doi:10.1073/pnas.1609595113/-/DCSupplemental.

set by the summation of interactions between a dopant and all particles in the base crystal (14). Assuming that interactions between dopants are negligible, i.e., that the dopant concentration is low and the interstitial site occupancy approaches zero, this reduces to a simple transition-state theory for thermally activated jumps between neighboring minima in the energy landscape.

In a BCC crystal the minima in which interstitial impurities will reside are the tetrahedral sites (Fig. 1*B*, green spheres) (18). We can identify two transition paths between tetrahedral sites that are most likely to contribute to the motion of a dopant. The first one comprises the shortest path from one tetrahedral site to another (T–T transition) during which displacement the particle crosses a saddle point in the energy landscape. The second one (T–O–T transition) goes from a tetrahedral site through an octahedral site to an adjacent tetrahedral site (18). The rate at which these hops occur is governed by the energy barrier U_A separating two sites along either path.

We parameterize our simulations to match an experimental system of charged poly(methyl methacrylate) particles in an apolar solvent, which forms BCC crystals at low densities (19, 20). In these colloidal systems, the main control parameter is particle volume fraction ϕ. The crystals are formed from colloids with a diameter $\sigma_b = 1.8$ μm and doped with interstitial impurities with $\sigma_d = 0.9$ μm. The interactions are described by Yukawa potentials to map the simulated phase behavior as a function of ϕ onto that determined experimentally (Fig. S1 and *Materials and Methods*). For a perfect BCC lattice we can now compute the activation energy for both the T–T and T–O–T paths by summing the potential energy fields, taking long-ranged contributions into account. The BCC crystal exhibits a periodic network of energy minima (Fig. S2), which provides an efficient means for interstitial motion on large length scales (18). For the colloidal BCC crystal, the numerically enumerated transition energies are few to several $k_B T$ and the differences in activation energy between the T–T and T–O–T paths are small (symbols in Fig. 1*C*). To describe these data phenomenologically, we consider the difference between the summed potential field at the interstitial site where U exhibits a minimum and the transition maximum $U_A(\phi) = U_+(\phi) - U_-(\phi) = \epsilon\left(\frac{e^{-\kappa g_+ a(\phi)}}{g_+ a(\phi)} - \frac{e^{-\kappa g_- a(\phi)}}{g_- a(\phi)}\right)$, where $a(\phi) = (\frac{\pi}{3\phi})^{\frac{1}{3}}$ is the normalized lattice constant in units σ_b and the geometrical constants g_- and g_+ account for the potential energy fields at the minima and maxima, respectively. We use this empirical equation to fit the simulation data at discrete values of ϕ; with values of $g_+ = 0.348$, $g_- = 0.345$ for the T–T transition and $g_+ = 0.297$, and $g_- = 0.295$ for the T–O–T this relation describes our numerical calculation data well (lines in Fig. 1*C*).

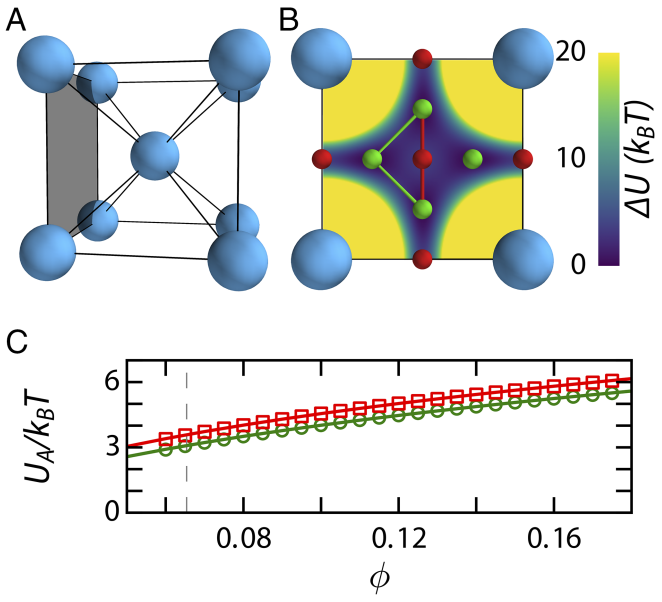

Fig. 1. (*A*) Schematic representation of a BCC unit cell. (*B*) The interstitial sites in a plane of the BCC unit cell with tetrahedral sites in green and octahedral sites in red. The T–T path (green) and T–O–T path (red) are indicated with lines connecting the interstitial sites. The potential field felt by the dopant is shown in the background. The values are the potential energy with respect to the global minimum at the tetrahedral site. Yellow indicates values of 20 k_BT and above. (*C*) Hopping barrier $U_A(\phi)$ along a T–T (circles) and a T–O–T (squares) path from numerical calculations. The solid lines are a parametric fit to $U_A(\phi)$ as described in the text, and the dashed line indicates the melting point ϕ_m.

Within the classical approach, the rate at which transitions occur is governed by a thermally activated process of the Eyring type: $k_h = k_{h,0}\exp(-U_A/k_B T)$. The Brownian attempt frequency is given by $k_{h,0}(\phi) = D_0/d_h^2(\phi) = k_B T/(d_h^2(\phi)6\pi\eta\sigma_d/2)$, in which d_h is the length of the transition path and D_0 is the self-diffusion coefficient of the interstitial impurities in a solvent of viscosity η. The long-time diffusion coefficient of the interstitial impurities as a function of volume fraction of the BCC crystal can now be predicted as $D_l(\phi) = d_h^2(\phi)k_h(\phi) = D_0\exp(-(U_A(\phi)/k_B T)^\beta)$ in which the stretch exponent β accounts for a distribution in hopping times due to the similar barriers of the two different transition paths.

To test the validity of this prediction based on classical transition-state theory, we simulate the Brownian dynamics of interstitial impurities within a static and perfect BCC crystal (Fig. 2*A*). The potential energy field experienced by the dopants exhibits clear minima at the tetrahedral sites (crosses, bottom of Fig. 2*G*). This leads to characteristic hopping dynamics in the trajectories of individual interstitial impurities, with particles vibrating within a tetrahedral site until they hop to a neighboring site (Fig. 3 *A* and *C*). Over time, the interstitial impurities probe the entire matrix by traveling through the interconnected network of local minima (Fig. S2). This action gives rise to a mean-squared displacement $\langle\Delta r^2(\tau)\rangle$ as shown in Fig. 4*B*, *Left*); at short times vibrations within the interstitial sites give rise to subdiffusive motion. This transitions into diffusive behavior at times longer than the Brownian self-diffusion time, $\tau \gg \tau_B$, as particles explore the lattice by hopping between interstitial sites; this is characterized by a long-time diffusion coefficient D_l (circles in Fig. 4*A* and Fig. S3). The simulation data for this static scenario are described very well by the prediction for $D_l(\phi)$ from transition-state theory, with $\beta = 0.61 \pm 0.01$ used as a fit parameter (line in Fig. 4*A*). The fact that β deviates from unity indicates a heterogeneous hopping process occurring via both the T–T and T–O–T transitions; the relative occurrence of T–T vs. T–O–T hops is expected to be 3.5:1 based on the difference in activation energies, taking into account the number of possible T–T and T–O–T transitions from a given tetrahedral site. We note that at this point, we have not established an exact and quantitative relationship between the value of β and the ratio of hops occurring via the two possible transition routes.

In real materials, at least one crucial assumption in this classical approach fails as the matrix in which dopants diffuse is also excited by thermal fluctuations. Especially for BCC crystals in close proximity to their melting point, where doped crystals are typically processed to induce ductility and malleability, these fluctuations are known to be strong (15). Allowing the BCC phase in these colloidal systems to fluctuate retains an on-average perfect structure as evident from distinct Bragg peaks in their structure factor (Fig. S4). However, snapshots of the instantaneous structure show significant deviations from a perfect lattice as particles displace significantly from their equilibrium

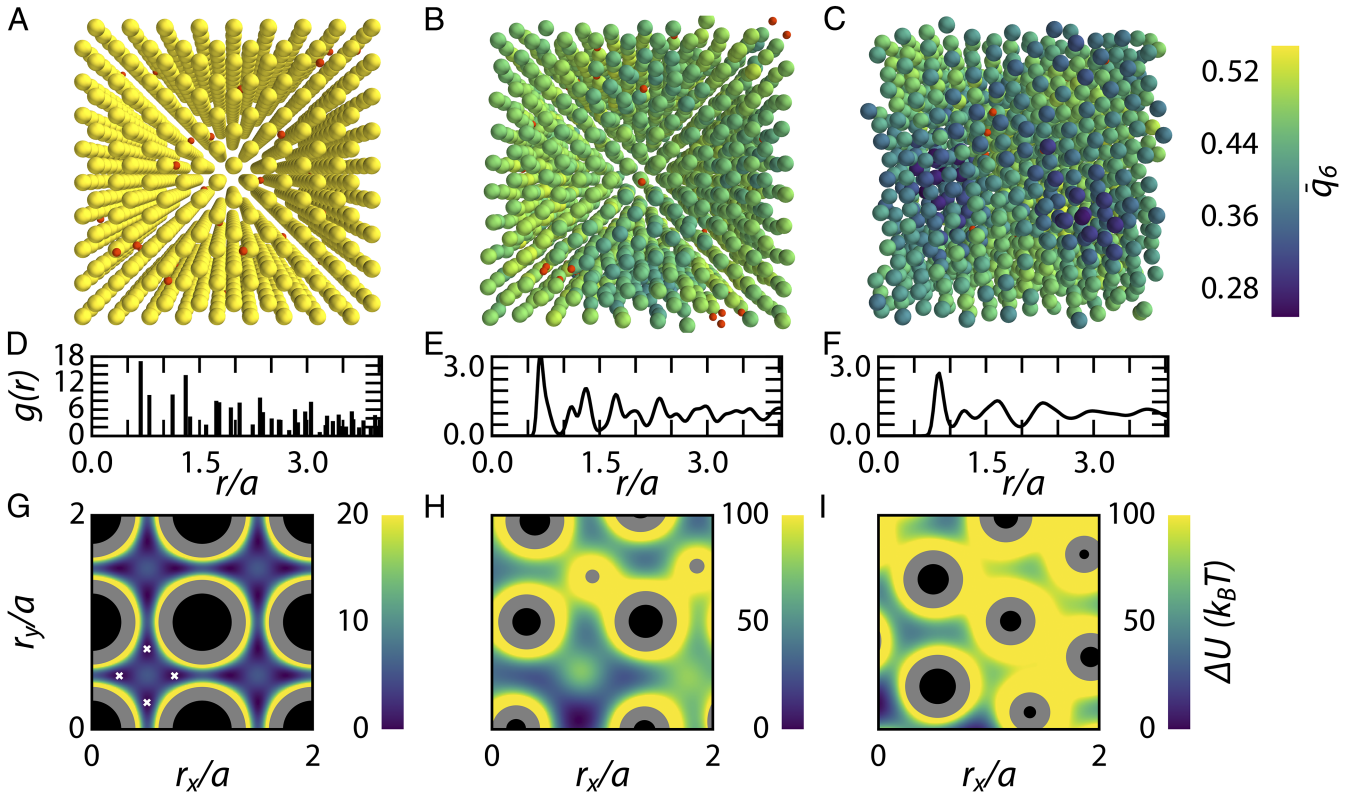

Fig. 2. Structural features of the BCC crystal for the simulation with a static (*A*, *D*, and *G*) and a dynamic (*B*, *E*, and *H*) base crystal and the experiments (*C*, *F*, and *I*). (*A*–*C*) Snapshots of BCC crystals at $\phi = 0.14$, in which particles are color coded according to their instantaneous bond-order parameter $\bar{q}_6$ and dopant particles are rendered in orange (*A* and *B* only). (*D*–*F*) Pair correlation functions $g(r)$. (*G*–*I*) Potential energy landscape through four unit cells within the on-average ordered lattice, where black disks indicate the hard-sphere radius of the base crystal particles and the gray areas indicate the volume, from which the center of mass of dopants is excluded, due to dopant–base particle overlap.

positions. Reconstructions of the system in which the particles are color coded according to their instantaneous bond-order parameter $\bar{q}_6$ (21) illustrate the significant amount of thermal disorder within these BCC crystals, both in silico and in experiments (Fig. 2 *B* and *C*). The thermally excited excursions of particles from their average lattice position translate into peak broadening in the pair-correlation function $g(r)$ (Fig. 2 *E* and *F*). We note that $g(r)$ for experiment and simulation are in excellent agreement, even though the field of view in our measurements is limited due to experimental constraints. Despite the strong thermal disorder in these fluctuating BCC crystals, it can still be structurally distinguished from a liquid by means of spherical harmonic bond-order parameters (Fig. S5), to probe local structure, and the existence of well-defined Bragg peaks in the structure factor (Fig. S4) that signals the presence of long-ranged order.

The effect of the instantaneous deviations from a perfect lattice due to thermal excitations becomes apparent when we plot a snapshot of the potential energy landscape that a dopant particle experiences at a given time. Instead of the regular landscape that exhibits minima at tetrahedral sites, the fluctuating BCC crystal presents an apparently disordered potential energy landscape (Fig. 2*H*) in which the variations in the height of energy barriers and the depth of localization wells are significantly larger compared with the perfect lattice. Also from experimental data we can reconstruct the potential energy landscape; we obtain the particle positions from 3D image stacks. Using the pair interaction potential obtained by inversion of pair correlation functions (22) and assuming pairwise additivity, we can compute the potential energy of inserting a dopant particle at a given location within the lattice. Also the energy landscapes reconstructed in this way from snapshots of the experimental system exhibit strong disorder (Fig. 2*I*).

This high degree of instantaneous disorder in the energy landscape results in very different interstitial dynamics from those predicted by the classical theory. The dopant particles are more strongly localized, and transitions between minima appear at much lower frequency compared with those in a static crystal (Fig. 3). As a consequence, the ensemble-averaged mean-square displacements exhibit a localization plateau that extends by several orders of magnitude (Fig. 4*B*, *Right*), resulting in a strongly reduced rate of diffusion at long times. To confirm that the interstitial mean-squared displacement converges to a diffusive behavior at long times, we run a longer simulation up to $2 \cdot 10^4\ \tau_B$; indeed the upturn we see in Fig. 4*B* becomes diffusive at even longer times (Fig. S3*C*).

To extract D_l from these data, we extrapolate the mean-squared displacement to infinite time; see *Fig. S3: Determination of the Long-Time Diffusion Coefficient* for a detailed description of our method. Allowing the crystal that surrounds the interstitial impurities to fluctuate results in more than two orders-of-magnitude reduction in the diffusion rate (blue symbols, Fig. 4*A*). Clearly, the effect of thermal excitations of the lattice cannot be ignored in describing dopant dynamics in BCC crystals.

Two possible contributions to this drastic reduction in interstitial diffusion rate can be identified. First, static or low-temperature BCC crystals feature a percolated path of T–T transitions, providing an efficient pathway for interstitial diffusion over large length scales (18). This percolated path results from the center-of-inversion symmetry of the BCC lattice. In the thermal BCC phase, especially close to melting, thermal excitations of the lattice are so pronounced that the instantaneous

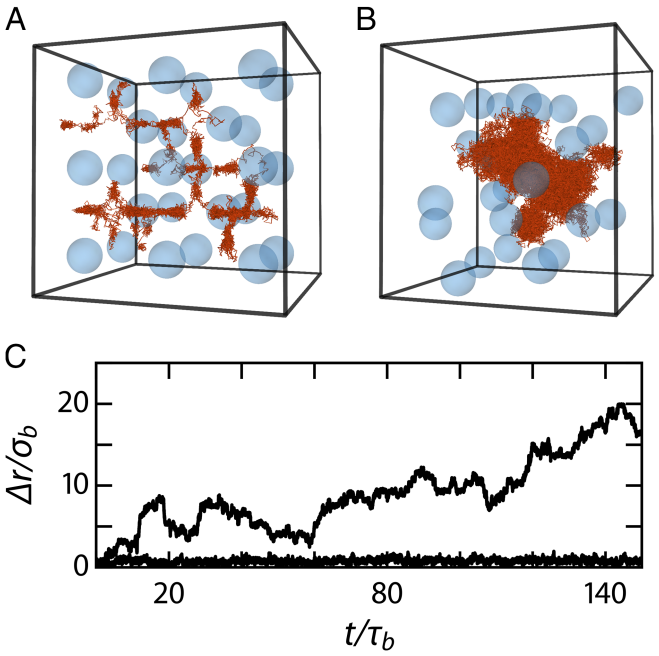

Fig. 3. (*A* and *B*) Trajectory of a single interstitial dopant in the crystalline matrix over $\Delta t = 29\ \tau_b$ in a static BCC crystal (*A*) and $\Delta t = 150\ \tau_b$ in a dynamic BCC crystal (*B*). (*C*) Interstitial displacement with respect to $t = 0$ in a static (bottom line) and a dynamic (top line) base crystal.

center-of-inversion symmetry is lost. Note that this applies only to instantaneous snapshots of the structure, whereas time averaging cancels out these fluctuations and restores the BCC symmetry, for example evidenced by the distinct Bragg peaks in the time-averaged structure factor (Fig. S4). As thermal fluctuations break the local and instantaneous symmetry, the percolated transition path that relies on this symmetry is also lost; this is evidenced in potential energy isosurfaces reconstructed from snapshots of the thermal BCC lattice in Fig. S2.

Second, as the potential energy landscape is strongly time varying, hopping now requires not only a fluctuation large enough to escape a local minimum, but also the simultaneous availability of a low-energy pathway that remains open during the transition event. In effect, two competing frequencies come into play: (*i*) that of escape attempts of the dopant and (*ii*) the frequency with which the potential energy landscape reconfigures. As the Brownian time scales of the base crystal and the dopants do not differ by much due to the moderate size asymmetry, escape events now become cooperative and thus significantly less likely. It is known that the effect of fluctuating barriers on hopping is strongly nonmonotonic and can lead to either enhancement, when the two frequencies become resonant, or reduction in transition rates (23, 24). As we work in the classical limit, where the transition itself is not instantaneous but requires a finite time, this poses the additional constraint that the path remains open for the duration of the transition event, which further slows down hopping. The combination of these events leads to a strong quenching of the interstitial mobility in fluctuations of BCC lattices.

A key feature for particles in disordered potential landscapes is the emergence of heterogeneous dynamics. To investigate this, we plot the time-averaged $\langle \Delta r^2 \rangle$ for all interstitial particles individually. For the static crystal, no heterogeneities in particle dynamics are observed, with all mean-squared displacements collapsing onto the ensemble average (Fig. 4*B*, *Left*). By contrast, for the fluctuating BCC crystal, strongly heterogeneous dynamics are observed, with a large inhomogeneity in the single-particle behavior (Fig. 4*B*, *Right*).

To explore the origins of these distinct heterogeneous dynamics within an on-average ordered solid, we reconstruct snapshots of the interstitial positions. Whereas dopants are homogeneously distributed for the static crystal (Fig. 5*A*), they exhibit strong clustering in the fluctuating BCC over the entire range of base crystal densities ϕ (Fig. 5*B* and Fig. S6). We hypothesize that this clustering is caused by the lattice strain accompanying the insertion of a single interstitial impurity into a tetrahedral site. Clustering between interstitials minimizes the overall elastic deformation of the matrix and is thus energetically favorable. This gives rise to an emergent elastic attraction between the impurity particles. Similar lattice-strain–mediated interactions are well established to exist for crystallographic defects that cause a lattice deformation (25). Indeed, we observe a strong increase in the lattice strain, defined as the average displacement of base crystal particles from their equilibrium position $\Delta r_{b,l}$ normalized to the lattice constant a, as a function of the distance to a nearest impurity.

We observe that the clusters are highly dynamic, with spontaneous particle association and dissociation (Figs. S6–S8 and Movies S1 and S2). This indicates a dynamic equilibrium between singlets (S) and bound states (B) $nS \rightleftharpoons B_n$, in which the association constant depends on the effective attractive potential U_{eff} emerging through the elasticity of the matrix: $k_a \propto \exp(U_{eff}/k_B T)$. We observe a significant fraction of singlets in stable coexistence with clusters, which does not evolve over time after equilibrating our simulation system (Fig. S9). This suggests that the effective attraction strength is of the order of the thermal energy $k_B T$: the dynamic equilibrium between clusters and singlets resulting from a balance between the configurational entropy of distributing impurities across the lattice and the enthalpic gain upon forming a cluster. This is further corroborated by the distribution of cluster sizes $P(S_C)$ (Fig. 5*F*). These data are well described by an exponential decay as indicated by

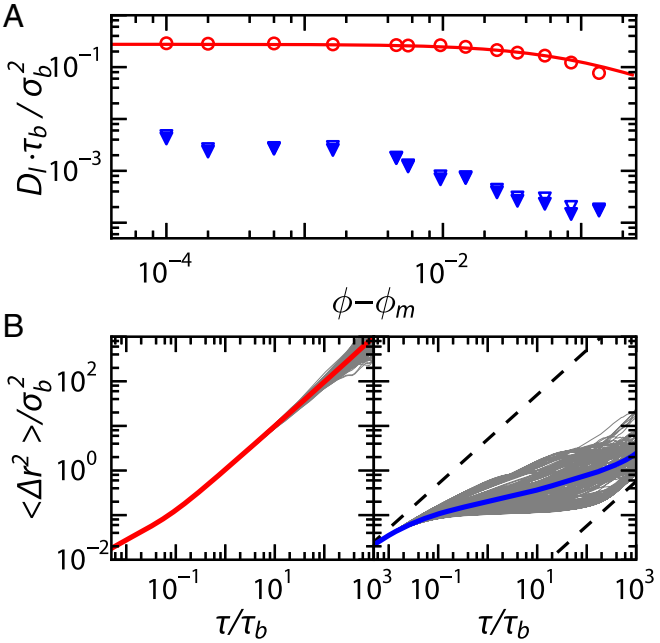

Fig. 4. (*A*) Long-time diffusion coefficients D_l as a function of distance to the melting point $\phi - \phi_m$ for static (circles) and dynamic (triangles) crystals, with $\phi_m = 0.061$ as determined in Fig. S1. Open symbols indicate D_l determined from the mean-squared displacements at $\tau = 5 \cdot 10^2 \tau_b$, whereas solid symbols are computed by extrapolating $\langle \Delta r^2 \rangle$ to infinity. The solid line is a fit to the transition-state prediction for $D_l(\phi)$, as described in the text. (*B*) $\langle \Delta r^2 \rangle$ for individual particles, with the ensemble-average $\langle \Delta r^2 \rangle$ (thick line) superposed for a fixed (*Left*) and a dynamic (*Right*) crystal.

the solid line in Fig. 5*F*. This indicates that clusters are formed by an open association process governed by a dynamic reaction equilibrium between unimeric dopants and clusters.

Intuitively, one may expect that particles present in an attractive cluster of dopants would exhibit lower mobility than their singlet counterparts as their local density is higher. Surprisingly, we observe the opposite; trajectories of dopants reveal that the degree of localization is in fact reduced for particles in clusters compared with singlets within the same lattice (Fig. 5*D*). To determine the origins of this counterintuitive observation, we determine the instantaneous deviation of particle positions away from their equilibrium site in the lattice $\Delta r_{b,l}$ as a function of the distance to the nearest dopant $\Delta r_{b,d}/a$. Especially for low-volume fractions, where deviations from classical transition-state theory are large, we observe a strong increase in the lattice strain in proximity to a dopant (Fig. 5*E*) whereas the average orientational bond-order $\bar{q}_6$ is maintained (Fig. S5). This result suggests that dopant particles, especially those present in clusters, locally weaken the lattice, resulting in larger mobility for both the dopants and the surrounding crystalline matrix. Interestingly, the fact that deviations in the dynamics of interstitial impurities are exacerbated close to the melting transition is also observed in the carbon-doped BCC phase of iron (12).

In this paper we demonstrated how thermal fluctuations can lead to the failure of classical theories for dopant dynamics and give rise to complex heterogeneous and anomalous dynamics within an on-average ordered matrix. Large instantaneous deviations from a perfect lattice due to thermal excitations cause a disordered potential energy landscape in which interstitial atom diffusion can be orders of magnitude slower than expected based on transition-state theory. Our simulations also give rise to a microscopic picture of the strongly heterogeneous dynamics of interstitial dopants: Elastic interactions between dopants cause them to agglomerate within the lattice, which in turn locally softens the matrix and gives rise to enhanced mobility. The coupling between spatial organization of the dopants, the local properties of the matrix, and resulting dopant dynamics can be expected to play a crucial role in the effective tailoring of material properties using doping. Arriving at a complete description of these complex dynamics would require extension of classical lattice dynamics to account for both the fluctuating and locally disordered energy landscapes, for which a framework was developed for glasses (24), and for the emergent interactions and spatial inhomogeneity of the dopants.

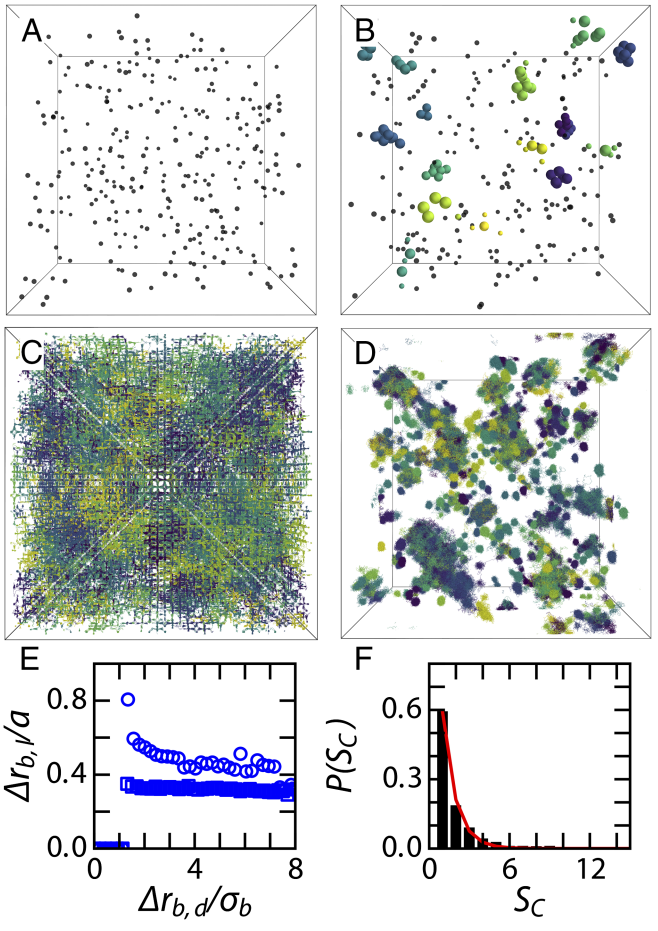

Fig. 5. (*A* and *B*) Dopant positions in a snapshot at $\phi = 0.07$, in which particles belonging to the same cluster are color matched, whereas singlets are displayed in gray for static (*A*) and dynamic (*B*) base crystals. (*C* and *D*) Particle trajectories of all particles over a time interval of $2 \cdot 10^3 \tau_b$ for static (*C*) and dynamic (*D*) base crystals. (*E*) Lattice strain $\Delta r_{b,l}/a$, taken as the average deviation of particle positions with respect to their equilibrium site, as a function of distance to a dopant for $\phi = 0.07$ (circles) and 0.12 (squares). (*F*) Distribution of cluster sizes $P(S_C)$ for $\phi = 0.07$, fitted with an exponential distribution $P(S_C) \propto e^{-S_C/S_C^*}$ with $S_c^* = 0.96$ the characteristic cluster size (red line).

Materials and Methods

Simulations. We perform Brownian dynamics simulations using HOOMD-BLUE, a GPU accelerated software package, in single-precision mode (26, 27). Analysis routines are all written in the python programming language, using scipy, (28) numpy (29), lmfit (30), scikit-learn (31), matplotlib (32), and mayavi (33) libraries. For the calculation of bond-order parameters we use BondOrderAnalysis (21) and we calculate Voronoi cells using the voro++ package (34). All quantities are expressed in normalized units, in terms of base particle diameter σ_b, base particle self-diffusion time τ_b, and k_BT, respectively. All raw data and scripts can be accessed via https://github.com/sprakellab/dopantdynamics.

Simulations are performed in the canonical ensemble (or N,V,T system) with periodic boundaries. Systems consist of two types of particles, one that forms the crystalline matrix ($\sigma_b = 1.8$ μm) and the dopants ($\sigma_d = 0.9$ μm). This size ratio of 0.5 is experimentally accessible and close to that for carbon-doped iron and lithium impurities in silicon (35). The particles interact via Yukawa potentials parameterized using experimental data (see below). The simulations assume pairwise additivity of the potentials; in the experimental system of charged colloids many-body effects are known to occur (36). Nonetheless, in previous work we have established that pairwise additive BD simulations can capture the main behavior of experimental crystals of the charged colloids we simulate here (37).

Brownian dynamics integration, using the overdamped Langevin equations, is performed with a time step of $2.5 \cdot 10^{-5} \tau_b$, in one of two ways: Either both particle types are integrated for the dynamic crystal or only the dopant particles are subjected to integration for the static matrix. In all cases we simulate $N = 13{,}718$ base crystal particles. Dopant particles are placed randomly at tetrahedral interstitial sites in the pristine BCC lattice in a ratio of 1:47. Simulations are run for at least $2 \cdot 10^3 \tau_b$, preceded by an equilibration time of $2 \cdot 10^2 \tau_b$.

Experiments. Some aspects of the simulation results are experimentally verified by studying a system of polymethyl methacrylate particles, stabilized by polyhydroxystearic acid (20). Particles with diameters of $\sigma_b = 1.8$ μm and $\sigma_b = 0.9$ μm are prepared using established procedures (38). We suspend the particles in a density-matching solvent mixture of cis-decalin and tetrachloroethylene, in which 10 mM Aerosol OT is added to charge the particles (20). We image the samples in three dimensions and time using confocal fluorescence microscopy, using a VisiTech Infinity-3, mounted on a Nikon Ti-U and equipped with a Hamamatsu ORCA-Flash 4.0 camera. Three-dimensional volumes of 50 × 50 × 30 μm^3 are acquired at 1 Hz. Particle centroid positions are determined and linked together in time, using well-established methods based on the fitting of a Gaussian curve (39).

Mapping. The particles in the simulation interact via the Yukawa potential $U(r)/k_BT = \epsilon \frac{\exp(-\kappa\sigma(\frac{r}{\sigma}-1))}{r/\sigma}$. In the solvent we use, the inverse screening length κ is determined to be $1.8/\sigma_b$ (20). To define the interaction strength

ϵ we map the simulation data onto the experimentally determined melting point of the BCC crystal (Fig. S1). An $\epsilon_{b,b}$ of 713 gives a melting point at a volume fraction ϕ of 0.061 in silico, close to the melting point found experimentally, $\phi = 0.060$. For the smaller dopants we assume a particle-size independent surface charge density such that $\epsilon_{d,d} = 227$. The cross-interactions between dopant and matrix are taken as the average of the base–base interaction and the dopant–dopant interaction ($\epsilon_{b,d} = 470$). Data analysis methods are described in *Supporting Information*.

1. Pei QX, Zhang YW, Sha ZD, Shenoy VB (2013) Tuning the thermal conductivity of silicene with tensile strain and isotopic doping: A molecular dynamics study. *J Appl Phys* 114(3):033526.
2. Gaumé R, Viana B, Vivien D, Roger JP, Fournier D (2003) A simple model for the prediction of thermal conductivity in pure and doped insulating crystals. *Appl Phys Lett* 83(7):1355.
3. Kenyon AJ (2002) Recent developments in rare-earth doped materials for optoelectronics. *Progr Quant Electron* 26(4-5):225–284.
4. Macfarlane DR, Huang J, Forsyth M (1999) Lithium-doped plastic crystal electrolytes exhibiting fast ion conduction for secondary batteries. *Nature* 402:792–794.
5. Hentschel HGE, Moshe M, Procaccia I, Samwer K, Sharon E (2015) Microalloying and the mechanical properties of amorphous solids. *arXiv*:1510.03108.
6. Homan CG (1964) Diffusion of carbon in alpha iron. *Acta Metall* 12(9):1071–1079.
7. Farraro R, McLellan RB (1979) The diffusion of heavy interstitial solute atoms in body-centered cubic metals. *Mater Sci Eng* 39(1):47–56.
8. Weller M (2006) The Snoek relaxation in bcc metals-From steel wire to meteorites. *Mater Sci Eng* 442(1-2):21–30.
9. Tapasa K, Barashev AV, Bacon DJ, Osetsky YN (2007) Computer simulation of carbon diffusion and vacancy-carbon interaction in alpha-iron. *Acta Mater* 55(1):1–11.
10. Xiao R, Li H, Chen L (2015) High-throughput design and optimization of fast lithium ion conductors by the combination of bond-valence method and density functional theory. *Sci Rep* 5:14227.
11. Kang J, Chung H, Doh C, Kang B, Han B (2015) Integrated study of first principles calculations and experimental measurements for Li-ionic conductivity in Al-doped solid-state LiGe2(PO4)3 electrolyte. *J Power Sourc* 293:11–16.
12. da Silva JRG, McLellan RB (1976) Diffusion of carbon and nitrogen in B.C.C. iron. *Mater Sci Eng* 26(1):83–87.
13. Ramamoorthy M, Pantelides S (1996) Complex dynamical phenomena in heavily arsenic doped silicon. *Phys Rev Lett* 76(25):4753–4756.
14. Wert CA (1950) Diffusion coefficient of C in α-iron. *Phys Rev* 79(4):601–605.
15. Cahn RW, Haasen P (1996) *Physical Metallurgy* (Elsevier Science, Amsterdam).
16. Sentjabrskaja T, et al. (2016) Anomalous dynamics of intruders in a crowded environment of mobile obstacles. *Nat Commun* 7:11133.
17. Evers F, et al. (2013) Colloids in light fields: Particle dynamics in random and periodic energy landscapes. *Eur Phys J Spec Top* 222(11):2995–3009.
18. Wang Y, et al. (2015) Design principles for solid-state lithium superionic conductors. *Nat Mater* 14:1026–1031.
19. Yethiraj A, van Blaaderen A (2003) A colloidal model system with an interaction tunable from hard sphere to soft and dipolar. *Nature* 421(6922):513–517.
20. Kanai T, et al. (2015) Crystallization and reentrant melting of charged colloids in nonpolar solvents. *Phys Rev E Stat Nonlin Soft Matter Phys* 91(3):1–5.
21. Lechner W, Dellago C (2008) Accurate determination of crystal structures based on averaged local bond order parameters. *J Chem Phys* 129(11):114707.
22. Behrens SH, Grier DG (2001) Pair interaction of charged colloidal spheres near a charged wall. *Phys Rev E Stat Nonlin Soft Matter Phys* 64(5):050401.
23. Reimann P, Hänggi P (1997) Surmounting fluctuating barriers: Basic concepts and results. *Stochastic Dynamics* (Springer, Berlin), Vol 484, pp 127–139.
24. Schweizer KS, Saltzman EJ (2004) Activated hopping, barrier fluctuations, and heterogeneity in glassy suspensions and liquids. *J Phys Chem B* 108(51):19729–19741.
25. Teodosiu C (2013) *Elastic Models of Crystal Defects* (Springer, Berlin).
26. Anderson JA, Lorenz CD, Travesset A (2008) General purpose molecular dynamics simulations fully implemented on graphics processing units. *J Comput Phys* 227(10): 5342–5359.
27. Glaser J, et al. (2015) Strong scaling of general-purpose molecular dynamics simulations on GPUs. *Comput Phys Comm* 192:97–107.
28. Jones E, Oliphant T, Peterson P (2001) SciPy: Open source scientific tools for Python. Available at https://www.scipy.org. Accessed November 4, 2016.
29. Van Der Walt S, Colbert SC, Varoquaux G (2011) The NumPy array: A structure for efficient numerical computation. *Comput Sci Eng* 13(2):22–30.
30. Newville M, Ingargiola A, Stensitzki T, Allen DB (2014) LMFIT: Non-linear least-square minimization and curve-fitting for Python, Technical Report. Available at https://zenodo.org/record/11813#.WCBMCPkrJph. Accessed June 15, 2016.
31. Pedregosa F, et al. (2011) Scikit-learn: Machine learning in Python Gaël Varoquaux. *J Mach Learn Res* 12:2825–2830.
32. Hunter JD (2007) Matplotlib: A 2d graphics environment. *Comput Sci Eng* 9(3):90–95.
33. Ramachandran P, Varoquaux G (2011) Mayavi: 3D visualization of scientific data. *Comput Sci Eng* 13(2):40–51.
34. Rycroft C (2009) Voro++: A three-dimensional voronoi cell library in C++. *Chaos* 19(4):041111.
35. Slater JC (1964) Atomic radii in crystals. *J Chem Phys* 41(10):3199.
36. Merrill JW, Sainis SK, Dufresne ER (2009) Many-body electrostatic forces between colloidal particles at vanishing ionic strength. *Phys Rev Lett* 103:138301.
37. van der Meer B, et al. (2014) Highly cooperative stress relaxation in two-dimensional soft colloidal crystals. *Proc Natl Acad Sci USA* 111(43):15356–15361.
38. Antl L, et al. (1986) The preparation of poly(methyl methacrylate) lattices in non-aqueous media. *Colloid Surface* 17(1):67–78.
39. Gao Y, Kilfoil ML (2009) Accurate detection and complete tracking of large populations of features in three dimensions. *Optic Express* 17(6):4685.
40. Ester M, Kriegel HP, Sander J, Xu X (1996) A density-based algorithm for discovering clusters in large spatial databases with noise. *Proceedings of the Second International Conference on Knowledge Discovery and Data Mining*, eds Simoudis E, Han J, Fayyad U (AAAI Press, Portland, OR), pp 226–231.